RSC Advances

PAPER

View Article Online
View Journal | View Issue

Cite this: *RSC Adv.*, 2025, **15**, 45438

Enhancement of mechanical, corrosion, and biocompatibility properties of zinc alloys through magnesium and neodymium alloying for bone implant applications

Minghan Li,†[a] Zhaobo Zhu,†[c] Long Zhang,†[d] Shaoyu Hu,[b] Jiayi Li,[b] Suiou Li,[a] Xiaohua Jiang,[a] Baoxin Peng*[e] and Song Hao *[b]

Zinc (Zn) alloys, though beneficial for biodegradable applications due to their controlled degradation, biocompatibility, and potential to aid in bone healing, often suffer from inadequate mechanical properties. To enhance their performance, this study investigates the incorporation of magnesium (Mg) and neodymium (Nd) as alloying elements and applies hot extrusion to produce Zn-based alloys with superior mechanical and biological characteristics suitable for moderate load-bearing orthopedic uses. The resulting Zn-0.1Mg-1Nd alloy exhibits a fine-grained structure with an average grain size of 1.36 μm, which enhances its tensile strength from 71 MPa for pure Zn to 381 MPa for the alloy, alongside a notable increase in elongation from 10.7% to 17.7%. These improvements fulfill the mechanical requirements for biodegradable bone-fixation devices. Corrosion tests, including electrochemical and immersion assessments in simulated body fluid (SBF), demonstrate the alloy's enhanced degradation resistance, with the lowest corrosion rate recorded at 0.094 mm year^{-1}. Additionally, the Zn-Mg-Nd alloys show good biocompatibility, as evidenced by their favorable interactions with human bone marrow-derived mesenchymal stem cells (hBMSCs) and murine macrophages (RAW 264.7), and further promote osteogenic differentiation in hBMSCs. Overall, the Zn-Mg-Nd alloy system emerges as a promising candidate for biodegradable orthopedic applications.

Received 13th October 2025
Accepted 7th November 2025

DOI: 10.1039/d5ra07819a

rsc.li/rsc-advances

1 Introduction

With the increasing aging population, the demand for advanced biomedical materials tailored to elderly patients has become increasingly urgent. Zinc (Zn), an essential trace element distributed in human tissues and organs, has garnered significant interest in this context.[1,2] The recommended daily intake of Zn ranges from 8–11 mg for adults and approximately 2–3 mg for infants.[3] Importantly, the human body exhibits a high tolerance to excess Zn intake, ranging from 100 to150 mg day^{-1}.[4] It means that Zn can effectively return to physiological homeostasis following cessation of exposure. Owing to its favorable biocompatibility and suitable *in vivo* degradation rate, Zn is regarded as a strong candidate for next-generation biodegradable orthopedic implants.[5,6]

Nevertheless, pure Zn is inherently limited by poor mechanical performance, primarily attributed to the insufficient strengthening modes.[7–9] These characteristics compromise its ability to sustain load-bearing functions in clinical scenarios. Recent advancements have demonstrated that the mechanical properties of Zn can be significantly enhanced through strategic alloying with elements such as germanium (Ge),[10] magnesium (Mg),[11,12] calcium (Ca),[13,14] strontium (Sr),[15] lithium (Li),[16–18] silver (Ag),[19,20] copper (Cu),[21,22] manganese (Mn),[23,24] iron (Fe),[25,26] titanium (Ti),[27,28] and zirconium (Zr).[29–31] The effectiveness of these alloying strategies is further amplified by thermomechanical processing techniques, including rolling,[32] extrusion,[33] drawing,[34] equal channel angular pressing (ECAP),[35] and high-pressure torsion (HPT)[36] which refine the microstructure and enhance mechanical strength and ductility.

[a]*Spine Surgery Baiyun District People's Hospital of Guangzhou, Guangzhou, Guangdong, China*

[b]*Department of Spine Orthopedics, Zhuhai People's Hospital The Affiliated Hospital of Beijing Institute of Technology, Zhuhai Clinical Medical College of Jinan University, Zhuhai, 519000, China. E-mail: haosong527@126.com*

[c]*Department of Pediatric Orthopedic, Center for Orthopedic Surgery, The Third Affiliated Hospital of Southern Medical University, Guangzhou 510515, China*

[d]*Department of Orthopaedic Surgery, Guangzhou Key Laboratory of Spine Disease Prevention and Treatment, Guangdong Provincial Key Laboratory of Major Obstetric Diseases, Guangdong Provincial Clinical Research Center for Obstetrics and Gynecology, The Third Affiliated Hospital, Guangzhou Medical University, Guangzhou, 511495, China*

[e]*The State Key Laboratory of Respiratory Disease, Department of Otolaryngology, Head and Neck Surgery, Laboratory of ENT-HNS Disease, Guangzhou Institute of Respiratory Health, The First Affiliated Hospital, Guangzhou Medical University, Guangzhou 510120, China. E-mail: bxin_peng@163.com*

† These authors contributed equally: Minghan Li, Zhaobo Zhu, Long Zhang.

Among these alloying elements, Mg is particularly promising due to its excellent biosafety profile (375–500 mg day^{-1}).[4] Mg alloys have made a great progress in the orthopedic fields and been approved in clinic trial.[37,38] Prior studies support the efficacy of Mg alloying. For example, Jin *et al.* reported that minor addition of Mg (<0.1 wt%) into Zn-Mg alloys improves mechanical properties.[39] However, the tensile strength is still below 300 MPa that is unable to meet the mechanical requirements of biodegradable metals.[40,41] Increasing Mg content can improve mechanical strength of Zn-Mg alloys at the expense of ductility (<5%) due to the formation of brittle eutectic structure.[42,43] The lamellar eutectic structure promotes the stress concentration during cold deformation, which can be alleviated by refining into particles. Severe plastic deformations, like HPT and hydrostatic extrusion, are effective methods for complete refinement.[36,44] However, these processing methods are expansive and hard to produce bulk samples at large scale. Consequently, Zn-Mg alloys should avoid high fractions of eutectic structure to achieve high ductility through conventional extrusion. We finally select Zn-0.1(wt%) Mg alloys as a base and improve the mechanical properties by alloying with other elements.

Neodymium (Nd), a representative rare earth (RE) element, has also emerged as a beneficial additive in biodegradable Mg alloy systems.[45,46] Clinically, Nd-containing biodegradable alloys such as Mg-3Nd-0.2Zn-0.4Zr (JDBM) have demonstrated cortical bone-matching mechanical properties, excellent biocompatibility, and uniform degradation.[38] Beyond their structural benefits, Nd-containing compounds possess notable anti-inflammatory, antimicrobial, and anticancer properties, with Nd^{3+} ions shown to exert membrane-protective effects on healthy cells, further enhancing their biomedical utility.[47]

While the effects of rare earth elements such as neodymium (Nd) have been widely investigated in Mg alloy systems, their roles in Zn based alloys remain largely unexplored. To bridge this knowledge gap, we developed a series of Zn-Mg-Nd alloys using a casting process followed by hot extrusion. These alloys were systematically characterized in terms of microstructures, mechanical performance, corrosion behaviors, cytocompatibility, and osteogenesis. The objective was to comprehensively evaluate their suitability as biodegradable implants for orthopedic applications.

2 Experiments

2.1 Preparation and characterization of Zn alloys

Zn based alloys were synthesized using high-purity Zn (99.99 wt%), Mg (99.99 wt%), and Nd (99.95 wt%) metals. The elements were melted in a low-carbon steel crucible under a protective atmosphere composed of CO_2 and SF_6 at a volume ratio of 99 : 1 to minimize oxidation. The resulting molten alloy was subsequently poured into a cylindrical copper mold with dimensions of 200 mm in length and 100 mm in diameter. Actual elemental compositions of the cast alloys were determined *via* inductively coupled plasma-mass spectrometry (ICP-MS), and the results are listed in Table 1. Cylindrical billets measuring 60 mm in diameter and 50 mm in length were machined from the cast ingots and used for extrusion. The hot extrusion process was carried out at 250 °C with a ram speed of 1 mm s^{-1} and an extrusion ratio of 36.

Table 1 Actual compositions of cast Zn alloys

	Chemical compositions (wt%)		
Alloys	Mg	Nd	Zn
Zn-0.1Mg	0.09	—	Basal
Zn-0.1Mg-0.5Nd	0.10	0.51	Basal
Zn-0.1Mg-1Nd	0.09	1.02	Basal

Scanning electron microscope (SEM) was utilized to characterize the microstructures of pure Zn and Zn alloys. Elemental mapping was conducted using an energy-dispersive spectroscopy (EDS) system (GENESIS 60S) integrated with the SEM. Prior to observation, all samples were subjected to standard metallographic preparation, including mechanical grinding, polishing, and chemical etching. The etchant comprised 4 wt% nitric acid dissolved in ethanol. To further investigate microstructural evolution before and after tensile deformation, electron backscatter diffraction (EBSD) and transmission electron microscope (TEM) analyses were performed. EBSD specimens were first mechanically ground and then electrochemically polished using a 10 vol% perchloric acid solution, with processing conditions maintained at −30 °C and 15 V. For TEM analysis, thin foils were prepared *via* twin-jet electropolishing in an electrolyte composed of 4 wt% perchloric acid in ethanol.

2.2 Tensile tests

Standard dog-bone-shaped tensile specimens were machined along the extrusion direction using electrical discharge machining (EDM). Prior to mechanical testing, all samples were ground to ensure uniform surface finish. Tensile experiments were conducted using a universal testing machine (Zwick/Roell Z100, Germany) at a constant strain rate of 1×10^{-3} s^{-1}. The gauge length for each specimen was set to 20 mm.

2.3 Electrochemical and immersion tests

Electrochemical measurements were performed using a CHI660C workstation configured with a conventional three-electrode system with an electrochemical cell.[48] Prior to testing, all specimens were ground with silicon carbide papers and polished using a diamond suspension to achieve a mirror-like finish. The exposed surface area of each sample in simulated body fluid (SBF) was 10 × 10 mm, and experiments were conducted at 37 °C. Potentiodynamic polarization (PDP) curves were recorded by sweeping the potential from −1.6 V to −0.5 V *versus* a saturated calomel electrode (SCE) at a scanning rate of 0.1 mV s^{-1}. The corrosion potential (E_{corr}) and corrosion current density (i_{corr}) were extracted from the PDP curves. Electrochemical impedance spectroscopy (EIS) was conducted at open-circuit potential (OCP) across a frequency range of 10^5 to 10^{-1} Hz with a 5 mV sinusoidal perturbation. For immersion testing, mechanically polished specimens were placed in centrifuge tubes filled with SBF,

maintaining a solution-to-exposed-area ratio of 20 mL cm^{-2}. After a 30 day immersion period, the samples were removed, rinsed with deionized water, and treated with a 200 g L^{-1} chromic acid solution to remove corrosion products. The corrosion rate (C, μm $year^{-1}$) was determined using the equation: $C = \Delta m/(\rho A t)$, where Δm is the mass loss (mg), ρ is the density (g cm^{-3}), A is the exposed area (cm^2), and t is the immersion time (years). Scanning Kelvin probe force microscopy (SKPFM) was employed to evaluate the surface potential differences between the Zn matrix and secondary phases. Measurements were carried out using a Dimension FastScan atomic force microscope (Bruker, USA) equipped with a scanning Kelvin probe. A Pt-Ir-coated silicon tip was calibrated against highly oriented pyrolytic graphite prior to analysis. Topographical images were captured in tapping mode, followed by an interleave scan performed 100 nm above the surface under alternating voltages to map the relative potential distribution across different microstructural regions.

2.4 Cell viability tests

Human bone marrow-derived mesenchymal stromal cells (hBMSCs, Cell Bank, Chinese Academy of Sciences) and mouse macrophage cell line RAW264.7 (Cell Bank, Chinese Academy of Sciences) were cultured in Dulbecco's Modified Eagle Medium (DMEM, Gibco), supplemented with 10% fetal bovine serum (FBS), at 37 °C in a humidified atmosphere containing 5% CO_2. Before culturing, the disc samples used for preparing extracts underwent mechanical grinding by using 800#, 1200#, and 2000# papers, respectively. According to ISO 10993-12:2012 guidelines, extracts were prepared by immersing samples (2.2 cm^2 exposed surface area) in DMEM for 72 hours at a surface-area-to-volume ratio of 1.25 cm^2 mL^{-1}. The resulting extracts were diluted to 50% for subsequent biological testing. Cell viability was evaluated using the Cell Counting Kit-8 (CCK-8) through an indirect contact assay. The cell viability is calculated from the equations: $CV = \frac{OD_e - OD_b}{OD_c - OD_b} \times 100\%$. Where OD_e is absorbance of experimental group, OD_c is the absorbance of control group, OD_b is the absorbance of blank group. Moreover, the ionic concentrations in the extracts were quantified using inductively coupled plasma mass spectrometry (ICP-MS, Thermo Fisher Scientific, USA). Cells were seeded into 96-well plates at a density of 2000 cells per well. After a 24 hour incubation to allow cell adhesion, the culture medium was replaced with the prepared diluted extracts. Cells were then incubated for an additional 72 hours, followed by the addition of 10 μL CCK-8 reagent per well. After 2 hours of incubation, absorbance was measured at 450 nm using a microplate reader (iMARK, Bio-Rad, USA). The concentrations of Zn and alloying element ions in the extracts were further confirmed using ICP-MS (Agilent 7700, USA).

To complement the viability assay, a live/dead staining assay was conducted to assess cytotoxic effects. hBMSCs and RAW264.7 cells were independently seeded in 96-well plates and co-cultured with extracts from pure Zn, Zn alloys, or PBS (control) for 24 hours. After incubation, wells were washed with PBS to remove residual extract. Cells were then stained with Calcein AM (1 μM) and propidium iodide (PI, 2 μg mL^{-1}) (Thermo Fisher Scientific, USA) for 15 minutes at room temperature. Following staining, live and death cells were observed using a fluorescence microscope (Olympus, Tokyo, Japan).

2.5 Osteogenesis-induction tests

Human bone marrow-derived mesenchymal stromal cells (hBMSCs) were seeded into 6-well plates at a density of 6×10^4 cells per well. Once the cells reached approximately 80% confluence, the culture medium was replaced with osteogenic induction medium containing 50% alloy extract. The medium was refreshed every 48 hours. Alkaline phosphatase (ALP) staining and alizarin red S (ARS) staining were performed on days 7 and 14, respectively, to assess early and late osteogenic differentiation. Staining outcomes were visualized and documented using a light microscope (Olympus Co., Ltd, Tokyo, Japan).

For immunofluorescence analysis, hBMSCs were cultured on coverslips placed in 24-well plates at a seeding density of 5000 cells per well. Upon reaching 80% confluence, the culture medium was similarly replaced with osteogenic medium containing 50% extract. After 7 days of induction, cells were rinsed with PBS, fixed in 4% paraformaldehyde for 15 minutes, permeabilized with 0.1% Triton X-100 for 10 minutes, and blocked with 10% bovine serum albumin (BSA) for 1 hour. Cells were then incubated overnight at 4 °C with a primary antibody against Runx2 (1 : 200 dilution, ab192256, Abcam, USA). The following day, cells were washed three times with PBS and incubated with a fluorescently labeled secondary antibody (1 : 500 dilution, Abcam, USA) for 1 hour at room temperature.

For gene expression analysis, hBMSCs were seeded in 6-well plates at the same density (6×10^4 cells/well) and cultured in osteogenic medium containing 50% extract for 10 days. Total RNA was isolated using the RNeasy Mini Kit (Qiagen, Germany), and its concentration and purity were assessed spectrophotometrically. From each group, 1 μg of RNA was reverse-transcribed into cDNA using the SuperScript™ III Reverse Transcriptase Kit (Thermo Fisher Scientific, USA). The reverse transcription protocol consisted of annealing at 65 °C for 5 minutes, cooling at 4 °C for 1 min, reverse transcription at 50 °C for 60 minutes, and enzyme inactivation at 70 °C for 15 minutes. Quantitative real-time PCR (qPCR) was performed using SYBR Premix Ex Taq II (2X) (Takara, Japan). Cycling conditions were as follows: initial denaturation at 95 °C for 30 seconds, followed by 40 cycles of denaturation at 95 °C for 5 seconds, and annealing/extension at 60 °C for 30 seconds. The expression levels of osteogenic markers Runx2, osteopontin (OPN), and collagen type I (COL1) were quantified using GAPDH as the housekeeping gene. Relative gene expression was analyzed using the ΔΔCt method with a real-time PCR system.

2.6 Statistical analysis

Data were presented as the mean ± standard deviation from at least four independent sample. Statistical analysis was performed using one-way analysis of variance (ANOVA) in Prism software.

3 Results

3.1 Microstructures of Zn alloys

The microstructural features of as-deformed pure Zn and its alloys are presented in Fig. 1. In unalloyed Zn, numerous grains are delineated by distinct boundaries, with most grain sizes exceeding 50 μm. As shown in Fig. 1(b), the introduction of a small amount of Mg effectively refined the grain structure. Based on the Zn-Mg phase diagram,[39] the maximum solubility of Mg in Zn is approximately 0.1 wt%, which accounts for the absence of secondary phases in the as-deformed Zn-0.1Mg alloy. Incorporating Nd into the Zn-0.1Mg alloy facilitated the formation of secondary phase particles in Zn-0.1Mg-0.5Nd and Zn-0.1Mg-1Nd alloys. Notably, in the Zn-0.1Mg-1Nd sample (Fig. 1(d)), these precipitates exhibited irregular morphologies and relatively large dimensions.

Elemental contents for representative areas of the as-deformed samples are displayed in Table 2. Point analysis by EDS revealed that Mg contents in regions 2, 3, and 5 were 0.11, 0.08, and 0.10 wt%, respectively, suggesting that Mg was predominantly dissolved within the Zn matrix. In contrast, region 6 showed an Nd content of 12.36 wt%. The atomic Zn-to-Nd ratio in the secondary phase of the Zn-0.1Mg-1Nd alloy was close to 11, consistent with the presence of $NdZn_{11}$ compounds as predicted by the Zn-Nd binary phase diagram.[49] The $NdZn_{11}$ particles in Zn-0.1Mg-0.5Nd measured approximately 5 μm, whereas those in Zn-0.1Mg-1Nd exceeded 15 μm in size.

Fig. 2 presents the inverse pole figure (IPF) and kernel average misorientation (KAM) maps of as-deformed pure Zn and its alloyed counterparts. In the IPF images (Fig. 2(a)), crystallographic orientations are visualized using color coding: basal planes appear in red, prismatic orientations in green, and pyramidal directions in blue. The texture evolution across samples is captured by the multiple of uniform distribution (MUD), which decreased progressively from 3.70 in pure Zn to 1.59 in Zn-0.1Mg-1Nd, indicating a shift toward a more randomized grain orientation. Grain size analysis revealed that unalloyed Zn exhibited an average size of 56.90 μm, as shown in Fig. 2(b). Upon alloying, this size was significantly refined to 14.66 μm in Zn-0.1Mg alloy, further reduced to 5.13 μm in Zn-0.1Mg-0.5Nd alloy, and reached 1.36 μm in Zn-0.1Mg-1Nd alloy. These observations confirm the grain refinement effect induced by Mg and Nd additions. The KAM mappings (Fig. 2(c)), commonly employed to estimate dislocation density (ρ), was applied using the relation $\rho = 2\theta/\mu b$, where θ represents the KAM angle and μ and b are material constants. The measured KAM values for pure Zn, Zn-0.1Mg, Zn-0.1Mg-0.5Nd, and Zn-0.1Mg-1Nd were 0.46°, 0.20°, 0.23°, and 0.17°, respectively. Corresponding dislocation densities were calculated as 2.64×10^{14} m^{-2}, 0.99×10^{14} m^{-2}, 1.12×10^{14} m^{-2}, and 0.84×10^{14} m^{-2}. These results demonstrate that alloying Zn with minor Mg and Nd effectively reduces both grain size and dislocation density, thereby altering the deformation behavior of the material.

Table 2 Chemical compositions of selected areas in Fig. 1

	Chemical compositions (wt%)		
Areas	Mg	Nd	Zn
1	0	0	100
2	0.11	0	99.89
3	0.08	0	99.92
4	0.02	12.36	87.62
5	0.10	0	99.90
6	0.01	17.87	82.12

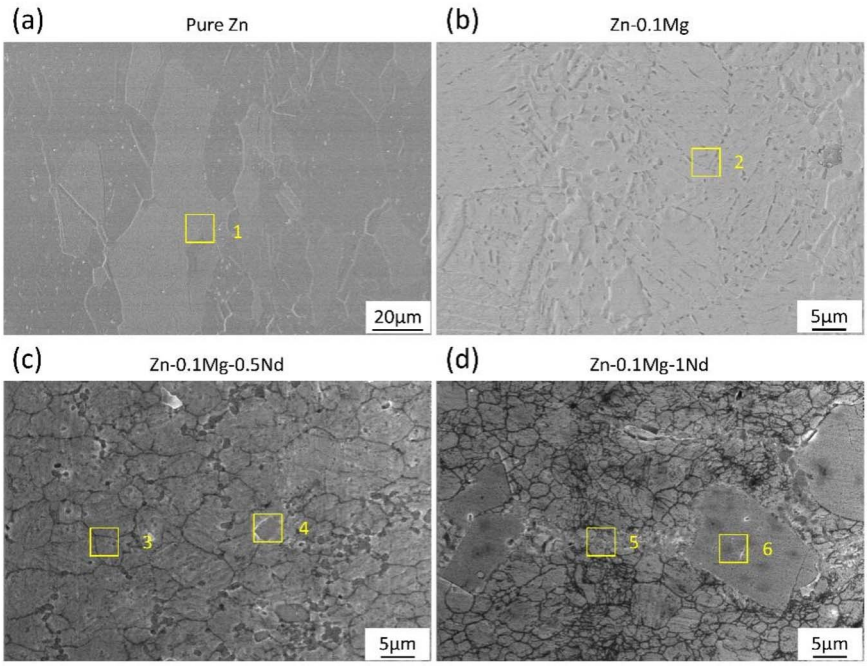

Fig. 1 Microstructures of as-deformed Zn-Li-Nd alloys. (a) Pure Zn; (b) Zn-0.1Mg alloy; (c) Zn-0.1Mg-0.5Nd alloy; (d) Zn-0.1Mg-1Nd alloy.

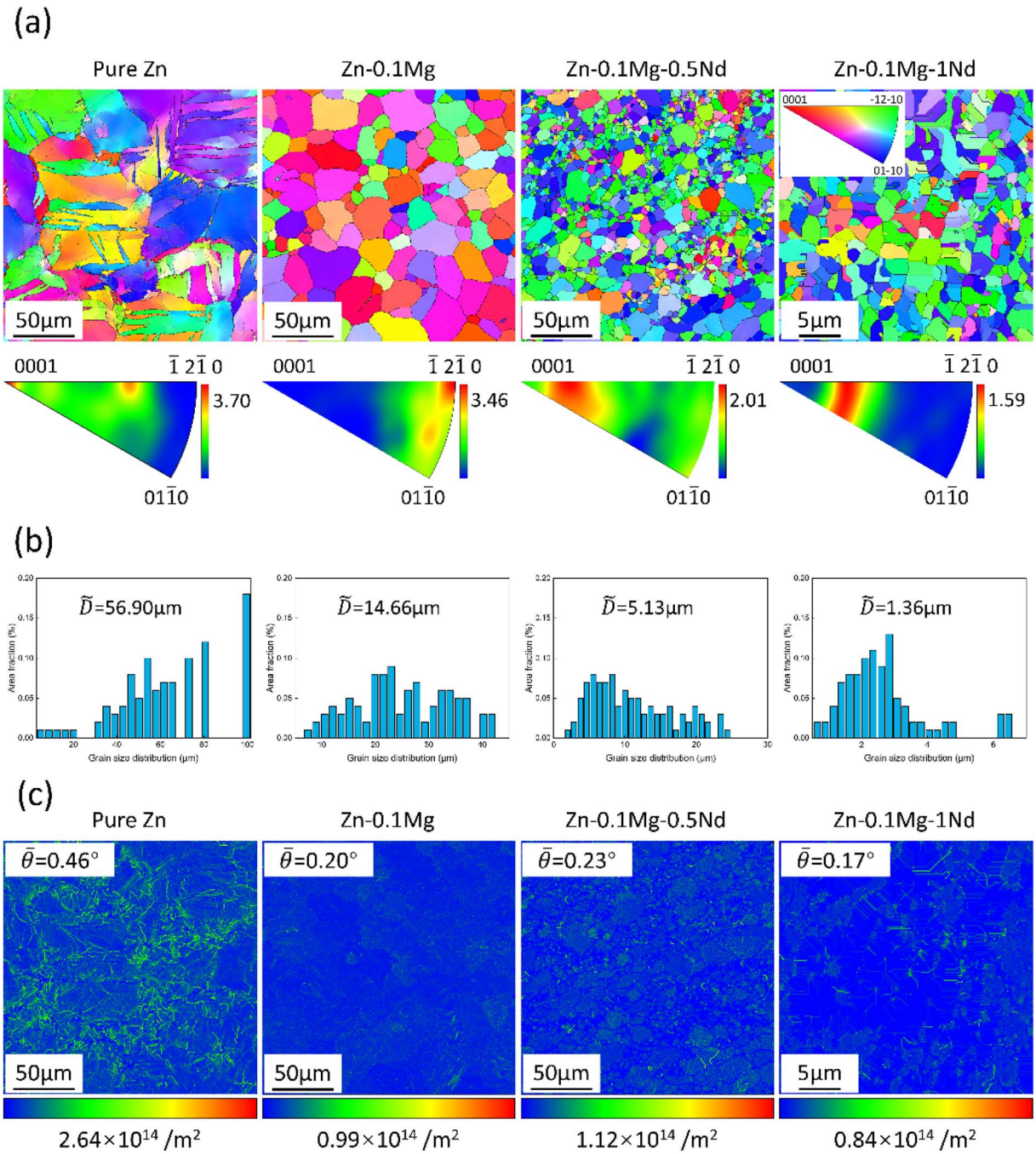

Fig. 2 EBSD analysis of as-deformed Zn-Mg-Nd alloys. (a) IPF mappings; (b) grain size distributions; (c) KAM mappings and dislocation densities.

The microstructure of the Zn-0.1Mg-1Nd alloy was further examined using TEM, as illustrated in Fig. 3. As shown in Fig. 3(a), submicron to micrometer-sized grains were observed, indicative of dynamic recrystallization (DRX) during thermo-mechanical processing. Fig. 3(b) and (c) reveal the morphology of precipitated secondary phases, which were identified as $NdZn_{11}$ through selected area electron diffraction (SAED) patterns. Additionally, elemental mapping *via* EDS confirmed a significant accumulation of Nd within these $NdZn_{11}$ particles, as displayed in Fig. 3(d).

3.2 Mechanical behaviors of pure Zn and Zn alloys

Fig. 4 summarizes the mechanical performance of pure Zn and Zn alloys, highlighting notable improvements in strength and ductility upon alloying. Pure Zn exhibited a tensile strength of 71 MPa and an elongation of 10.7%. With the addition of a small amount of Mg, the tensile strength markedly increased to 247 MPa, albeit with a reduced elongation of 7.1%. Further alloying with Nd resulted in tensile strengths of 315 MPa for Zn-0.1Mg-0.5Nd and 381 MPa for Zn-0.1Mg-1Nd, while elongations improved significantly to 9.5% and 17.7%, respectively. These

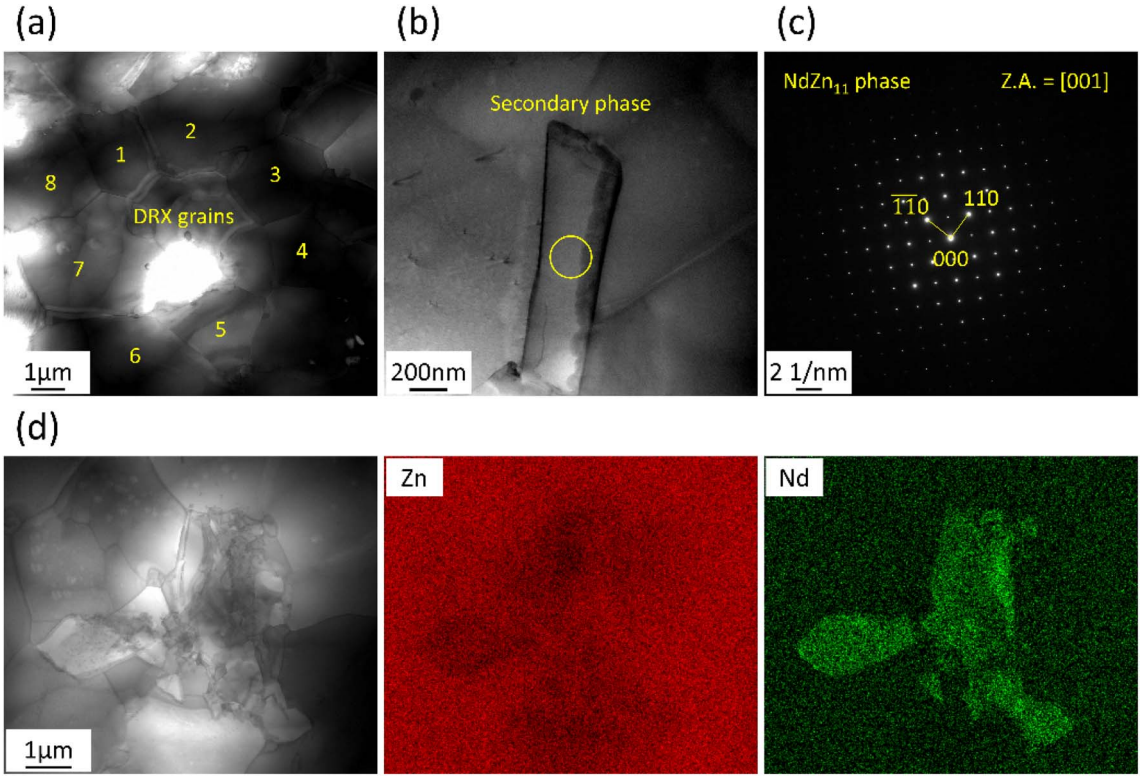

Fig. 3 TEM analysis of as-deformed Zn-Mg-Nd alloys. (a) DRX grains; (b) morphologies of secondary phases; (c) SAED image of $NdZn_{11}$ phase; (d) EDS mappings of $NdZn_{11}$ phase.

results confirm that the incorporation of Nd into Zn-Mg alloys effectively enhances both strength and plasticity. Fractographic examination (Fig. 4(c)) revealed ductile fracture features across all samples, with a growing density of dimples observed on the fracture surfaces as alloying increased. This microstructural evolution correlates well with the measured improvements in ductility.

3.3 Degradation behaviors of Zn alloys

Electrochemical corrosion behaviors of pure Zn and its alloys are illustrated in Fig. 5. E_{corr} and i_{corr} were extracted from the potentiodynamic polarization (PDP) curves *via* linear extrapolation of the cathodic branches, reflecting thermodynamic and kinetic aspects of corrosion, respectively. The E_{corr} value shifted from −1.14 V (*vs.* SCE) for pure Zn to −1.06 V for Zn-0.1Mg-1Nd, while i_{corr} decreased from 20.01 μA cm^{-2} (pure Zn) to 12.66 μA cm^{-2} (Zn-0.1Mg), and further declined to 12.34 μA cm^{-2} and 9.97 μA cm^{-2} in Zn-0.1Mg-0.5Nd and Zn-0.1Mg-1Nd, respectively. These findings indicate that alloying with Mg and Nd enhances corrosion resistance relative to pure Zn.

Fig. 5(b) presents the Nyquist plots for the investigated samples within the medium-to-low frequency range. Fitting the data with an equivalent electrical circuit (inset in Fig. 5(b)) revealed two distinct capacitive loops, corresponding to charge transport through the metal/oxide interface. Compared to pure Zn, Zn alloy samples displayed larger loop diameters, suggesting improved resistance to corrosion. This enhancement is attributed to the formation of a denser surface oxide layer, which inhibits charge transfer between the metal and simulated body fluid (SBF). The loop in the medium-frequency region reflects charge transport within the solid phase, while the low-frequency loop is associated with ion diffusion across the oxide film. Charge transfer resistance (R_{ct}) values, summarized in Table 3, were 1295 Ω cm^2 for pure Zn, and increased to 1896 Ω cm^2 and 1935 Ω cm^2 for Zn-0.1Mg-0.5Nd and Zn-0.1Mg-1Nd, respectively. Bode plots and phase angle distributions are shown in Fig. 5(c), further validating the enhanced corrosion resistance of the Zn alloys. The absolute impedance ($|Z|$) in the medium and low-frequency domains was higher for the alloys than for pure Zn, suggesting more effective barrier properties. The peak phase angle reached 60° for Zn-0.1Mg-1Nd, compared to 53° for pure Zn, indicating the presence of a more compact and protective corrosion layer on the alloy surface.[50]

Corrosion rates derived from mass loss measurements after 30 days of immersion are presented in Fig. 5(d). Pure Zn exhibited a corrosion rate of 0.186 mm $year^{-1}$. The incorporation of Mg reduced this rate to 0.155 mm $year^{-1}$ in the Zn-0.1Mg alloy. Further alloying with Nd resulted in a continued decline in corrosion rates, reaching 0.123 mm $year^{-1}$ for Zn-0.1Mg-0.5Nd and 0.094 mm $year^{-1}$ for Zn-0.1Mg-1Nd. These findings underscore the corrosion-mitigating effect of Mg and Nd additions.

Surface morphologies following immersion for 30 days are shown in Fig. 6(a). Both pure Zn and the alloy samples were covered by thick, particle-like corrosion products. Numerous cracks were visible across the surface layers, implying compromised barrier effectiveness. EDS elemental mapping and point analysis revealed a pronounced presence of carbon (C) in the

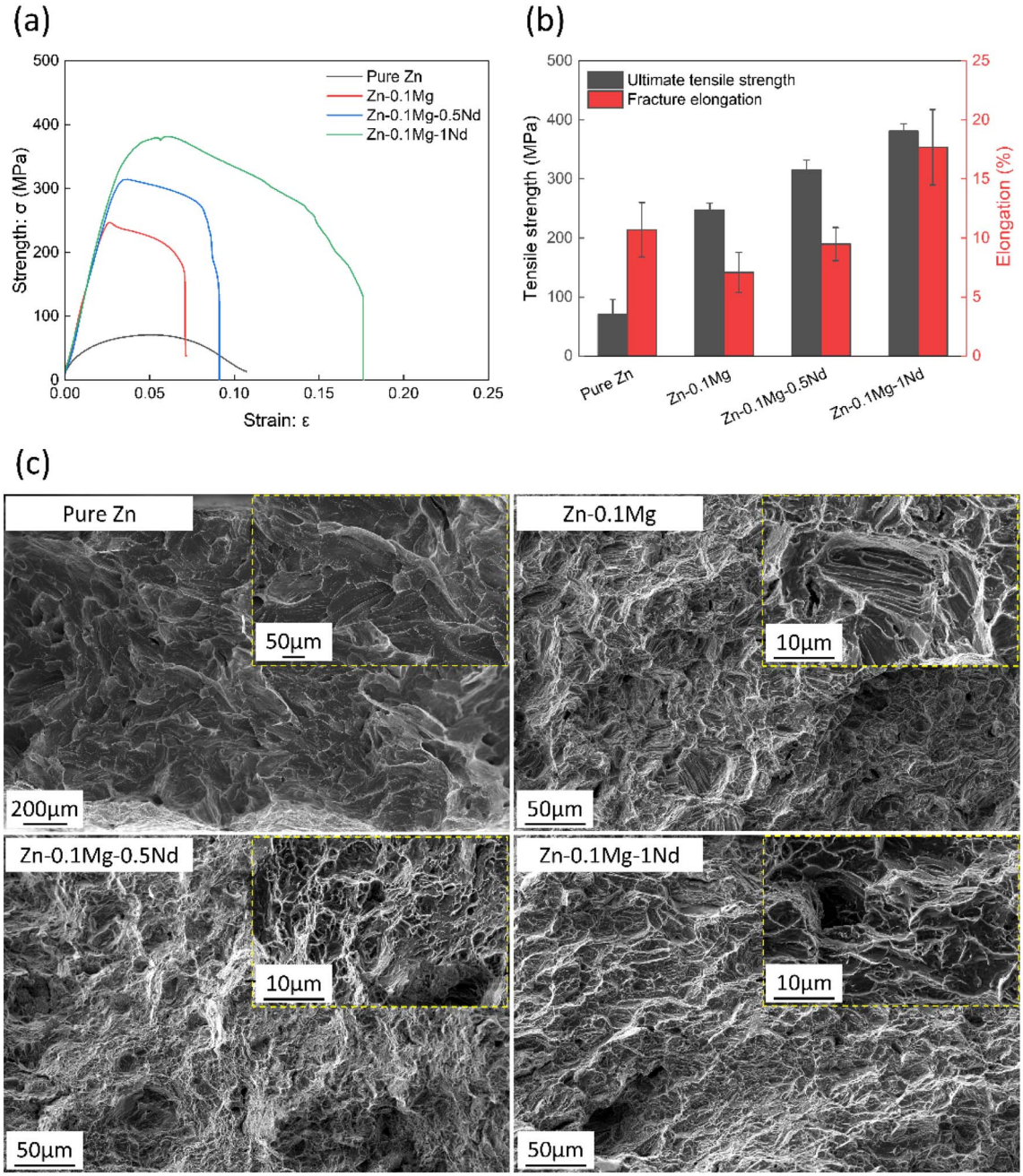

Fig. 4 Tensile behaviors of as-deformed Zn-Mg-Nd alloys. (a) Tensile curves; (b) Tensile strength and fracture elongations; (c) fracture morphologies.

corrosion layers. In contrast, adjacent areas showed considerably lower carbon content, often beneath that of oxygen (O). The elevated carbon levels are attributed to the precipitation of insoluble carbonate compounds formed by the interaction between carbonate ions in solution and metal cations on the surface.

Fig. 6(d) displays the substrate morphologies after the removal of surface corrosion products. Pure Zn exhibited signs of localized corrosion, while small pits (on the micrometer scale) were present on Zn-0.1Mg and Zn-0.1Mg-0.5Nd surfaces. In the Zn-0.1Mg-1Nd alloy, more complex degradation features emerged, including grain boundary attack and galvanic corrosion. These corrosive sites were predominantly located near $NdZn_{11}$ particles. The pronounced galvanic activity is linked to the electrochemical potential difference between the Zn matrix and $NdZn_{11}$ phases, as evidenced by scanning Kelvin probe force microscopy (SKPFM). Fig. 6(c) reveals the surface potential distribution and topography of Zn-0.1Mg-1Nd. The $NdZn_{11}$ regions exhibited a potential approximately 68.7 mV lower than the surrounding Zn matrix. This potential disparity facilitates micro-galvanic coupling in simulated body fluid (SBF), thereby accelerating localized corrosion at phase boundaries.

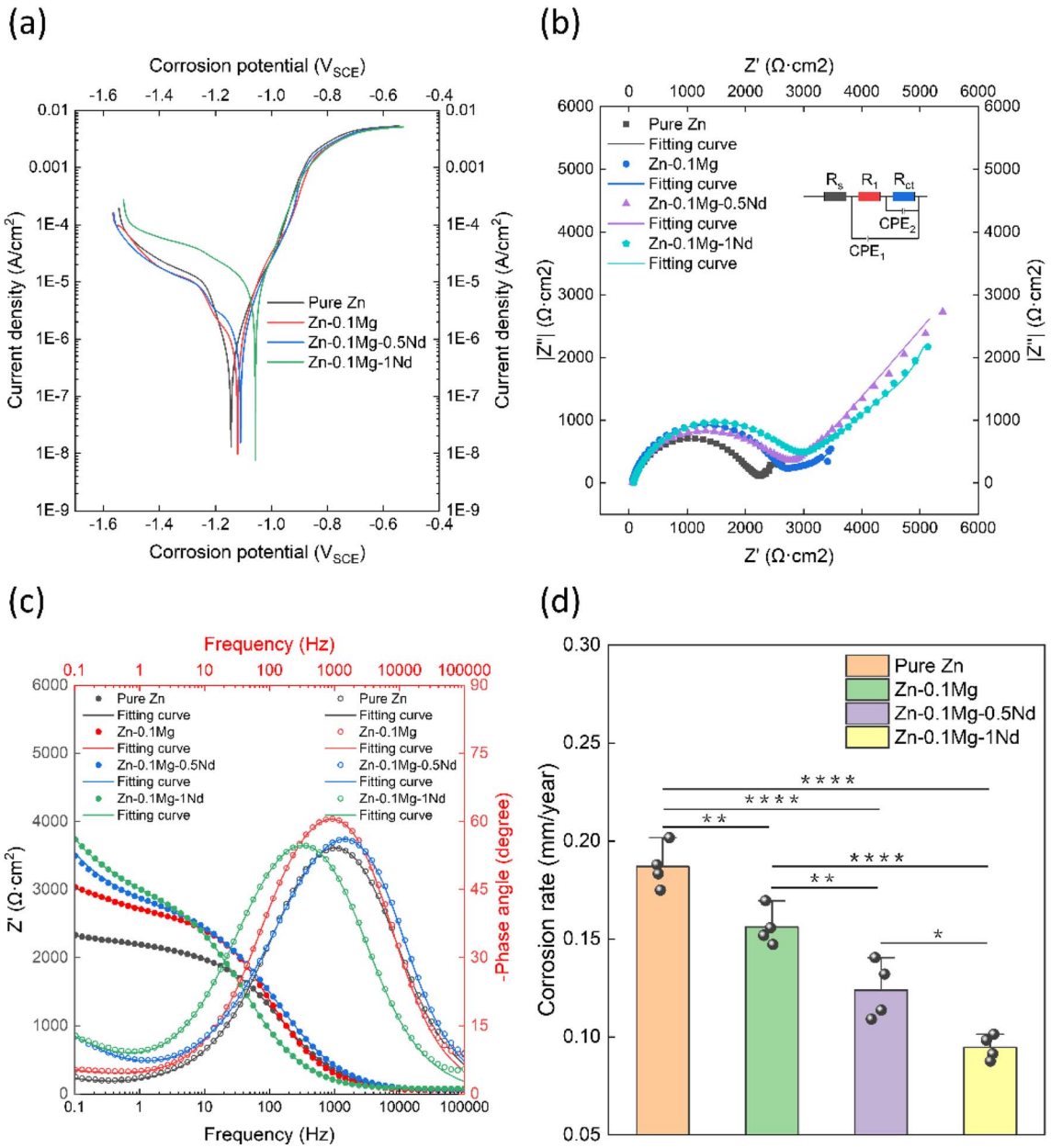

Fig. 5 Degradation behaviors of as-deformed Zn-Mg-Nd alloys. (a) PDP curves; (b) Nyquist plots and fitting curves; (c) Bode plots and phase angles; (d) corrosion rate measured by weight loss.

3.4 Biocompatibility of Zn alloys

Ionic concentrations in the alloy extracts were quantified and are depicted in Fig. 7(a). The extract from pure Zn showed the highest Zn ion content at 13.39 mg L^{-1}, while lower concentrations were recorded for Zn-0.1Mg (10.37 mg L^{-1}), Zn-0.1Mg-0.5Nd (9.95 mg L^{-1}), and Zn-0.1Mg-1Nd (9.78 mg L^{-1}). The

Table 3 Fitting parameters of the Nyquist plots

Circuit elements		Zn	Zn-0.1Mg	Zn-0.1Mg-0.5Nd	Zn-0.1Mg-1Nd
R_s (Ω cm^2)		63.49	54.09	62.36	76.85
R_1 (Ω cm^2)		894	1274	855	866
R_{ct} (Ω cm^2)		1295	1065	1896	1935
CPE_1	T (10^{-6} Ω^{-1} cm^{-2} s^n)	2.01	1.37	1.02	4.47
	$n1$	0.83	0.89	0.88	0.82
CPE_{dl}	T (10^{-6} Ω^{-1} cm^{-2} s^n)	30.98	6.33	17.04	34.67
	$n2$	0.38	0.68	0.52	0.59

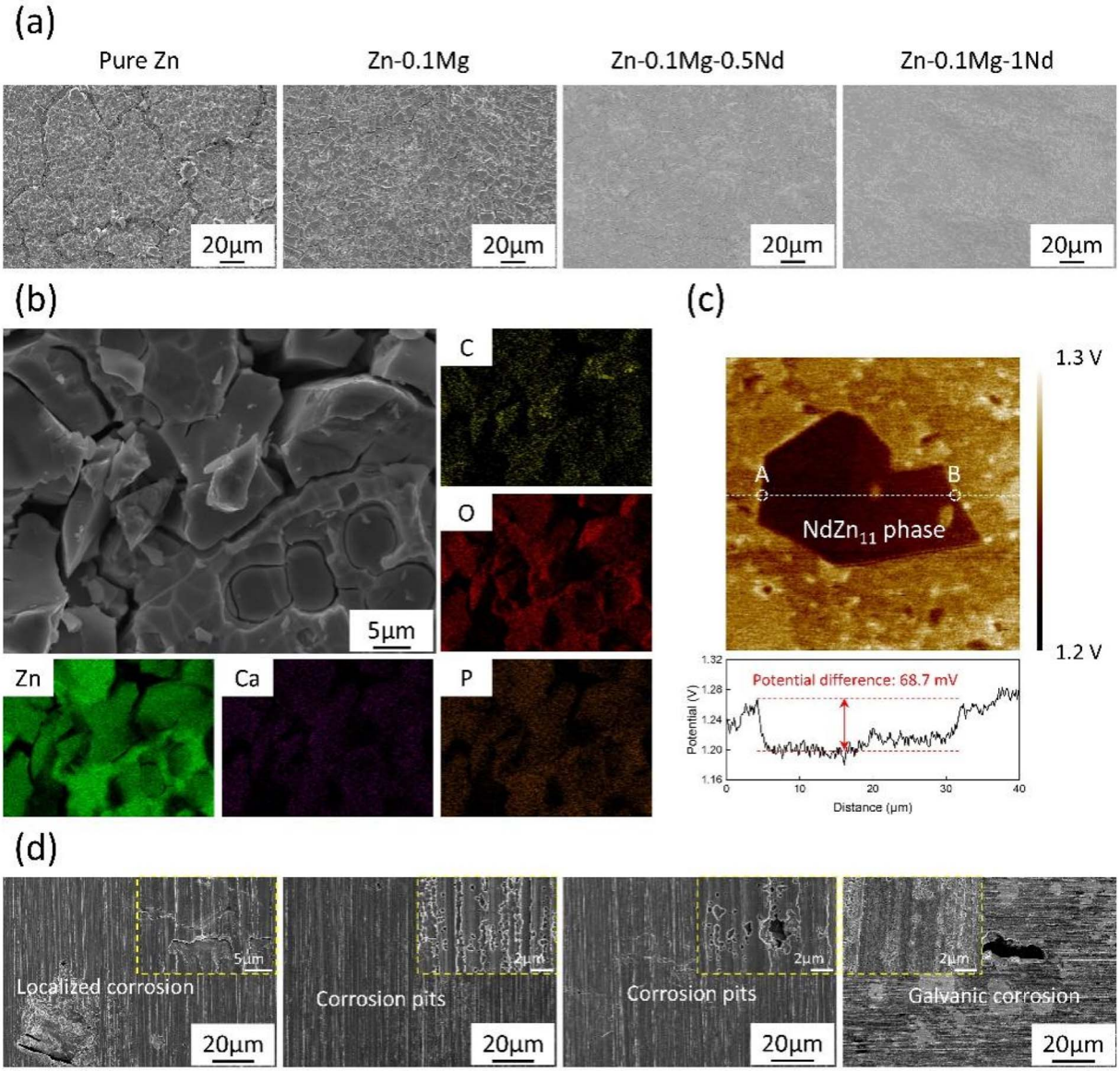

Fig. 6 Corrosion morphologies of as-deformed Zn-Mg-Nd alloys. (a) Morphologies of corrosion products on the surface of samples; (b) EDS mapping of corrosion products; (c) potential difference mapping; (d) surface morphologies of samples after removing corrosion products.

presence of Nd also significantly suppressed Mg ion release, which decreased from 4.58 mg L^{-1} in Zn-0.1Mg to 2.58 mg L^{-1} and 2.22 mg L^{-1} in Zn-0.1Mg-0.5Nd and Zn-0.1Mg-1Nd, respectively. A modest increase in Nd ion release was noted, rising from 0.07 mg L^{-1} in Zn-0.1Mg-0.5Nd to 0.1 mg L^{-1} in Zn-0.1Mg-1Nd.

Cell viability assessments of hBMSCs and RAW 264.7 macrophages cultured in the extracts are shown in Fig. 7(b). Undiluted extracts (100%) from the pure Zn group exhibited pronounced cytotoxicity. Upon one-fold dilution, the biocompatibility of all samples improved substantially. Notably, the Zn-Mg-Nd alloys supported cell viability levels exceeding 80%, suggesting a non-toxic response at this concentration. These values were comparable to the control group, indicating that the cells gradually adapted to the ionic environment. Among the two cell types, hBMSCs demonstrated greater tolerance to the extracts. After dilution, all alloy groups exhibited good cytocompatibility toward mesenchymal stem cells.

Live/dead fluorescence staining results from direct contact assays are presented in Fig. 7(c). The live hBMSCs and RAW264.7 cells are counted by Image J software, as shown in Fig. 7(d). In the control group, both cell types exhibited excellent adherence and spreading. Conversely, pure Zn and alloyed samples showed reduced attachment of RAW 264.7 cells. However, Zn-0.1Mg-Nd alloys supported a higher number of live hBMSCs, highlighting the positive impact of Nd incorporation on biocompatibility.

3.5 *In vitro* osteogenesis of Zn alloys

Gene expression analysis of key osteogenic markers (ALP, OPN, COL-1, and Runx-2) is presented in Fig. 8(a). Compared with both pure Zn and the untreated control, the Zn alloy groups

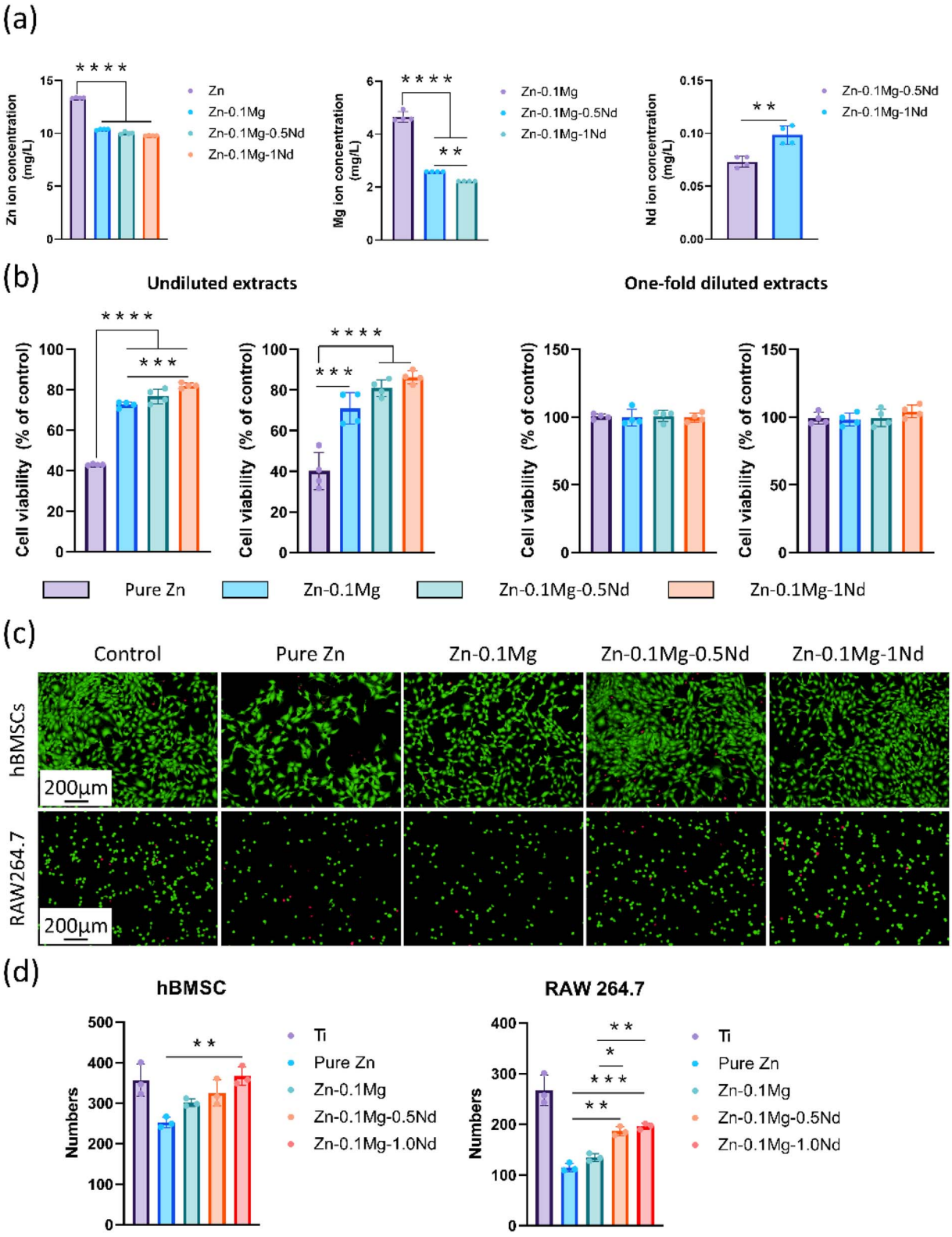

Fig. 7 Cytocompatibility of Zn alloys. (a) Ion concentrations in undiluted extracts; (b) cell viabilities of hBMSC and RAW264.7 cells; (c) live/dead staining images. (d) The numbers of live cells. *p < 0.05, **p < 0.01, ***p < 0.001, and ***p < 0.0001.

exhibited significantly elevated expression levels across all markers. Specifically, the ALP gene expression in the Zn-0.1Mg-1Nd group reached 6.75, more than double that of Zn-0.1Mg (2.41). Similarly, OPN expression increased from 1.89 to 4.31, and Runx-2 rose from 2.26 to 4.85, indicating enhanced osteogenic differentiation with Nd addition.

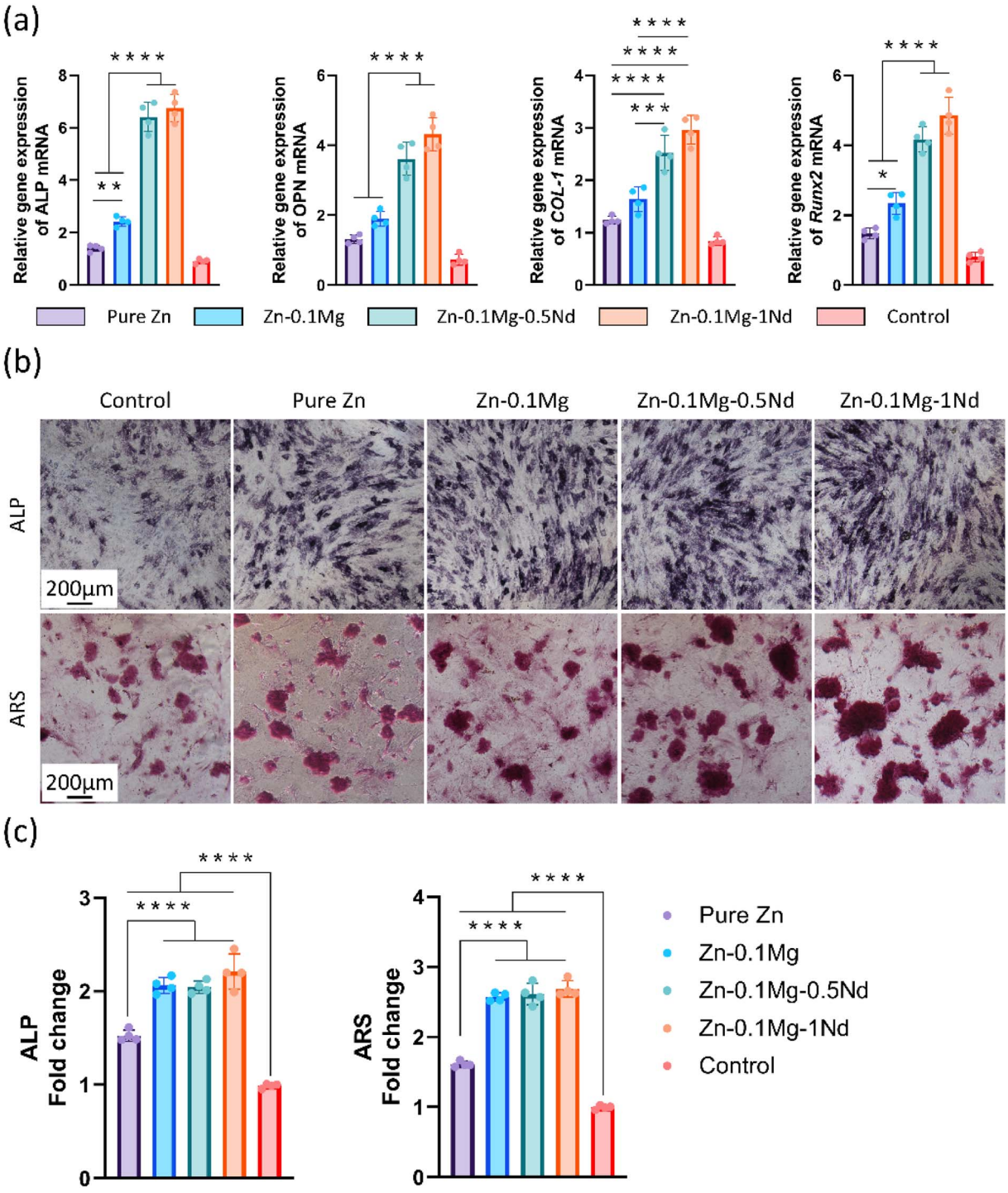

Fig. 8 Osteogenesis of Zn alloys. (a) q-PCR analysis; (b) ALP and ARS staining images; (c) ALP and ARS quantitative results. $^{**}p < 0.001$ and $^{***}p < 0.0001$.

Osteogenic staining results are shown in Fig. 8(b), where ALP and alizarin red S were used to evaluate early and late markers of bone formation. The ALP-stained images revealed higher blue staining intensity in Nd-containing alloy groups, suggesting improved early-stage osteo-inductive potential. In the alizarin red-stained images, more abundant red calcium nodules were observed in the Nd-containing Zn alloys compared to both the pure Zn and control groups. These findings collectively suggest that Nd addition significantly enhances the osteogenic capacity of Zn-Mg alloys.

4 Discussions

Microstructures of Zn alloys demonstrate that the secondary phase is particle-like $NdZn_{11}$ phase, which plays a crucial role in refining grains. According to the previous studies, dynamic

recrystallization is the dominant mechanism to refine grains.[51,52] Moreover, high extrusion temperature promotes the grain growth by dynamic recovery. The final grain size of as-deformed Zn alloys is determined by the dynamic recrystallization and dynamic recovery. The grain size of pure Zn would be more than 10 μm despite of HPT deformation, which is attributed to the low homologous temperature.[53] Minor addition of Mg has a significant effect on reducing the grain size, depending on the strain and temperature.[54] In our study, processing at 250 °C substantially promotes the grain growth due to the absence of secondary phases. After introducing Nd into Zn-0.1Mg alloy, the precipitated $NdZn_{11}$ phases are thermally stable due to its high-melting-point.[55] These particles preferentially nucleate at grain boundaries during solidification, where they suppress dendritic growth and refine the microstructure *via* the particle-stimulated nucleation (PSN) mechanism.[56] SEM analysis reveals that both the volume fraction and size of $NdZn_{11}$ particles increase with Nd content. Predominantly located along grain boundaries, these secondary particles serve to obstruct dislocation motion, thereby contributing to enhanced mechanical strength through an Orowan-type strengthening mechanism.[57]

While hot-extruded Zn-0.1Mg alloys demonstrate higher strength than pure Zn, their mechanical performance remains insufficient for load-bearing biomedical applications such as bone implants. Owing to the absence of secondary phases in Zn-0.1Mg alloys, the enhanced strength is attributed to the solid solution strengthening and grain boundary strengthening. Strength contributions from solid solution in Zn-0.1Mg alloys is about 27 MPa according to the previous studies.[58] Moreover, Zn-RE phase diagrams demonstrate that there is no solubility of Nd, indicating the absence of solid solution strengthening from Nd.[49] Upon hot extrusion, Zn-Mg-Nd alloys undergo recovery, dynamic recrystallization, and grain growth-a process facilitated by their relatively low recrystallization temperature. Under constant extrusion parameters, the final grain size is largely governed by the extent of grain boundary migration, which is effectively impeded by the presence of second-phase particles. The Hall–Petch relationship, $\sigma_y = \sigma_0 + kd^{-\frac{1}{2}}$, is used to calculate the strength contributions from grain refinement.[59] Where k is Hall–Petch coefficient, d is the average grain size. In Fig. 2, the average grain sizes of pure Zn reduce from 56.90 μm to 14.66 μm of Zn-0.1Mg alloy, then further to 1.36 μm of Zn-0.1Mg-1.0Nd alloy. Thus, strength contributions from grain refinement are 29 MPa for pure Zn, 80 MPa for Zn-0.1Mg alloy, 120 MPa for Zn-0.1Mg-0.5Nd alloy, and 211 MPa for Zn-0.1Mg-1.0Nd alloy, respectively. A higher volume fraction of these particles correlates with a stronger pinning effect on boundary motion. Post-extrusion microstructures show that thermally stable rare-earth-rich phases, including $NdZn_{11}$, become fragmented and aligned along the extrusion direction, imparting additional dispersion and second-phase strengthening. Nonetheless, the presence of $NdZn_{11}$ effectively mitigated grain coarsening during extrusion by suppressing grain boundary mobility. Collectively, the combined effects of grain refinement and second-phase dispersion substantially improved the mechanical performance-strength, ductility, and hardness-relative to unalloyed Zn.

The enhanced corrosion resistance observed with Nd addition arises from two primary mechanisms. First, grain refinement plays a pivotal role: smaller grains decrease the thermodynamic driving force for corrosion, thereby enhancing the integrity of the passive layer. This leads to corrosion modes within Zn matrix transfer from pitting corrosion to grain boundary corrosion, as shown in Fig. 6(d). As a result, the Zn-0.1Mg-0.5Nd and Zn-0.1Mg-1Nd alloys exhibited lower degradation rates of 0.123 mm $year^{-1}$ and 0.094 mm $year^{-1}$, respectively, compared to 0.186 mm $year^{-1}$ for pure Zn and 0.155 mm $year^{-1}$ for Zn-0.1Mg. Second, electrochemical differences introduced by Nd further modulate corrosion behavior. The standard electrode potential of Nd (−2.282 V) is considerably more negative than that of Zn (−0.762 V), rendering the low potential of $NdZn_{11}$ phase (as shown in Fig. 6(c)). This potential disparity facilitates micro-galvanic coupling between the α-Zn matrix and $NdZn_{11}$ phases, where the latter act as anodic sites. As Nd content increases, more $NdZn_{11}$ particles accumulate along grain boundaries, elevating the density of galvanic pairs. Despite localized galvanic activity, the overall corrosion resistance improves, primarily due to the synergistic effects of grain refinement and the formation of a more homogeneous and protective surface film.[60]

Ensuring favorable biocompatibility is critical for the clinical translation of biodegradable bone implants. Cell viabilities of hBMSCs and RAW264.7 cells are low for undiluted pure Zn extracts, while high cell viability in Zn alloys extracts, as shown in Fig. 7(b). This is because the tolerance of Zn ion concentration to cells is limited Low Zn ion concentration promotes cell proliferation and differentiation, while high value inhibits cell growth or even induces apoptosis.[61].The diluted pure Zn and Zn alloys extracts show negligible cytotoxicity, yielding cytotoxicity grades of 0 to 1 according to ASTM F895 standard. Although higher extract concentrations induced stronger cytotoxic responses for pure Zn extracts, all Zn-Mg-Nd groups promoted cellular proliferation, with viabilities exceeding 80%, indicating enhanced compatibility relative to Zn-0.1Mg alone. These findings suggest that the Nd-containing Zn alloys may be more suitable for clinical applications. Notably, the observed cytotoxic thresholds appear to correlate closely with Zn ion concentrations. While low levels (<4 μM) are known to support osteoblast viability, elevated concentrations (>300 μM) can impair fibroblast survival.[62] Thus, the optimized ion release profile in Zn-Mg-Nd alloys likely underpins their superior cytocompatibility and supports their promise as advanced candidates for biodegradable bone implants.

5 Conclusions

This study investigated the effects of Nd addition on the mechanical performance, corrosion behavior, cytocompatibility, and osteogenic potential of Zn-0.1Mg-xNd (x = 0.5, 1 wt%) alloys for biodegradable bone implants. The main findings are summarized as follows:

1. The average grain size of pure Zn (56.90 μm) was significantly refined to 14.66 μm in Zn-0.1Mg, 5.13 μm in Zn-0.1Mg-0.5Nd, and further to 1.36 μm in Zn-0.1Mg-1Nd alloys. Nd addition facilitated the formation of particle-shaped NdZn11 phases, which increased in size with higher Nd content.

2. The as-deformed Zn alloys exhibited markedly enhanced tensile strengths compared to pure Zn, reaching a maximum of 381 MPa. Elongation improved with increasing Nd concentration, with Zn-0.1Mg-1Nd demonstrating the highest ductility of 17.7% among all tested alloys.

3. Corrosion rates measured by electrochemical and immersion methods decreased upon Nd incorporation. Zn-0.1Mg-1Nd showed a notably low corrosion rate of 0.094 mm $year^{-1}$ after 30 days immersion in SBF. Corrosion behavior transitioned from localized corrosion in pure Zn to pitting in Zn-0.1Mg and Zn-0.1Mg-0.5Nd, and further to grain boundary and galvanic corrosion in Zn-0.1Mg-1Nd.

4. Extracts at 50% concentration from both pure Zn and Zn alloys exhibited negligible cytotoxicity toward hBMSCs and RAW 264.7 cells. Among the alloys, Zn-0.1Mg-1Nd showed the strongest promotion of osteogenic differentiation.

Conflicts of interest

The authors declare no competing interests.

Data availability

The datasets used and analysed during the current study available from the corresponding author on reasonable request.

Acknowledgements

The authors are grateful for funding from the President's Fund of Nanfang Hospital Baiyun Branch (Baiyun District People's Hospital, Guangzhou City) (BYYZ23014) and the Science and Technology Project (Baiyun District, Guangzhou City) (2024-YL-005).

References

1 M. Stefanidou, C. Maravelias, A. Dona and C. Spiliopoulou, Zinc: a multipurpose trace element, *Arch. Toxicol.*, 2006, **80**, 1–9, DOI: 10.1007/s00204-005-0009-5.

2 H. Tapiero and K. D. Tew, Trace elements in human physiology and pathology: zinc and metallothioneins, *Biomed. Pharmacother.*, 2003, **57**, 399–411, DOI: 10.1016/S0753-3322(03)00081-7.

3 P. Trumbo, S. Schlicker, A. A. Yates and M. Poos, Dietary Reference Intakes for Energy, Carbohydrate, Fiber, Fat, Fatty Acids, Cholesterol, Protein and Amino Acids, *J. Am. Diet. Assoc.*, 2002, **102**, 1621–1630, DOI: 10.1016/S0002-8223(02)90346-9.

4 J.-M. Seitz, M. Durisin, J. Goldman and J. W. Drelich, Recent Advances in Biodegradable Metals for Medical Sutures: A Critical Review, *Adv. Healthcare Mater.*, 2015, **4**, 1915–1936, DOI: 10.1002/adhm.201500189.

5 H. Yang, *et al.*, Evolution of the degradation mechanism of pure zinc stent in the one-year study of rabbit abdominal aorta model, *Biomaterials*, 2017, **145**, 92–105, DOI: 10.1016/j.biomaterials.2017.08.022.

6 P. K. Bowen, J. Drelich and J. Goldman, Zinc exhibits ideal physiological corrosion behavior for bioabsorbable stents, *Adv. Mater.*, 2013, **25**, 2577–2582, DOI: 10.1002/adma.201300226.

7 K. Chen, *et al.*, Effect of strain on degradation behaviors of WE43, Fe and Zn wires, *Acta Biomater.*, 2020, **113**, 627–645, DOI: 10.1016/j.actbio.2020.06.028.

8 B. Srinivasarao, A. P. Zhilyaev, T. G. Langdon and M. T. Pérez-Prado, On the relation between the microstructure and the mechanical behavior of pure Zn processed by high pressure torsion, *Mater. Sci. Eng., A*, 2013, **562**, 196–202, DOI: 10.1016/j.msea.2012.11.027.

9 D. Wu, T. Huang and Z. Liu, Mechanical response of high purity Zn wires with different diameters, *Mater. Lett.*, 2022, **324**, 132635, DOI: 10.1016/j.matlet.2022.132635.

10 K. Chen, *et al.*, A metal-semimetal Zn–Ge alloy with modified biodegradation behavior and enhanced osteogenic activity mediated by eutectic Ge phases-induced microgalvanic cells, *Biomaterials*, 2025, **321**, 123343, DOI: 10.1016/j.biomaterials.2025.123343.

11 H. Liu, *et al.*, Evolution of Mg–Zn second phases during ECAP at different processing temperatures and its impact on mechanical properties of Zn-1.6Mg (wt.%) alloys, *J. Alloys Compd.*, 2019, **811**, 151987, DOI: 10.1016/j.jallcom.2019.151987.

12 D. Zhao, *et al.*, Material–Structure–Function Integrated Additive Manufacturing of Degradable Metallic Bone Implants for Load-Bearing Applications, *Adv. Funct. Mater.*, 2023, **33**, 2213128, DOI: 10.1002/adfm.202213128.

13 X.-M. Li, *et al.*, Highly plastic Zn-0.3Ca alloy for guided bone regeneration membrane: Breaking the trade-off between antibacterial ability and biocompatibility, *Bioact. Mater.*, 2024, **42**, 550–572, DOI: 10.1016/j.bioactmat.2024.08.049.

14 Y. Zou, X. Chen and B. Chen, Effects of Ca concentration on degradation behavior of Zn-x Ca alloys in Hank's solution, *Mater. Lett.*, 2018, **218**, 193–196, DOI: 10.1016/j.matlet.2018.02.018.

15 B. Jia, *et al.*, Biodegradable Zn-Sr alloy for bone regeneration in rat femoral condyle defect model: In vitro and in vivo studies, *Bioact. Mater.*, 2021, **6**, 1588–1604, DOI: 10.1016/j.bioactmat.2020.11.007.

16 H. Yang, *et al.*, Zn-0.4Li alloy shows great potential for the fixation and healing of bone fractures at load-bearing sites, *Chem. Eng. J.*, 2021, **417**, 129317, DOI: 10.1016/j.cej.2021.129317.

17 Z. Zhang, *et al.*, Biodegradable ZnLiCa ternary alloys for critical-sized bone defect regeneration at load-bearing sites: In vitro and in vivo studies, *Bioact. Mater.*, 2021, **6**, 3999–4013, DOI: 10.1016/j.bioactmat.2021.03.045.

18 G. Li, D. Chen, Y. Mine, K. Takashima and Y. Zheng, Fatigue behavior of biodegradable Zn-Li binary alloys in air and simulated body fluid with pure Zn as control, *Acta*

Biomater., 2023, **168**, 637–649, DOI: 10.1016/j.actbio.2023.07.030.

19 R. J. Guillory, *et al.*, Improved biocompatibility of Zn-Ag-based stent materials by microstructure refinement, *Acta Biomater.*, 2022, **145**, 416–426, DOI: 10.1016/j.actbio.2022.03.047.

20 M. Sikora-Jasinska, *et al.*, Fabrication, mechanical properties and in vitro degradation behavior of newly developed ZnAg alloys for degradable implant applications, *Mater. Sci. Eng., C*, 2017, **77**, 1170–1181, DOI: 10.1016/j.msec.2017.04.023.

21 X. Qu, *et al.*, Biodegradable Zn-Cu alloys show antibacterial activity against MRSA bone infection by inhibiting pathogen adhesion and biofilm formation, *Acta Biomater.*, 2020, **117**, 400–417, DOI: 10.1016/j.actbio.2020.09.041.

22 Z. Tang, *et al.*, Potential biodegradable Zn-Cu binary alloys developed for cardiovascular implant applications, *J. Mech. Behav. Biomed. Mater.*, 2017, **72**, 182–191, DOI: 10.1016/j.jmbbm.2017.05.013.

23 S. Sun, *et al.*, Abnormal effect of Mn addition on the mechanical properties of as-extruded Zn alloys, *Mater. Sci. Eng., A*, 2017, **701**, 129–133, DOI: 10.1016/j.msea.2017.06.037.

24 G. Lu, *et al.*, Optimization of mechanical, corrosion properties and cytotoxicity of biodegradable Zn-Mn alloys by synergy of high-pressure solidification and cold rolling process, *J. Alloys Compd.*, 2024, **1005**, 175988, DOI: 10.1016/j.jallcom.2024.175988.

25 L. Ben Tzion-Mottye, *et al.*, The effect of slow strain rate tension and cyclic loading on biodegradable Zn–2%Fe–0.8%Mn alloy in a simulated physiological environment, *J. Mater. Res. Technol.*, 2023, **26**, 8527–8540, DOI: 10.1016/j.jmrt.2023.09.178.

26 Z. Z. Shi, *et al.*, Enhancement in mechanical and corrosion resistance properties of a biodegradable Zn-Fe alloy through second phase refinement, *Mater. Sci. Eng., C*, 2020, **116**, 111197, DOI: 10.1016/j.msec.2020.111197.

27 G. Boczkal, B. Mikulowski, I. Hünsche, C. G. Oertel and W. Skrotzki, Precipitation of intermetallic phase in Zn-Ti alloy single crystals, *Cryst. Res. Technol.*, 2008, **43**, 135–140, DOI: 10.1002/crat.200711068.

28 K. Wang, *et al.*, Binary Zn–Ti alloys for orthopedic applications: Corrosion and degradation behaviors, friction and wear performance, and cytotoxicity, *J. Mater. Sci. Technol.*, 2021, **74**, 216–229, DOI: 10.1016/j.jmst.2020.10.031.

29 Y. Su, *et al.*, Blending with transition metals improves bioresorbable zinc as better medical implants, *Bioact. Mater.*, 2023, **20**, 243–258, DOI: 10.1016/j.bioactmat.2022.05.033.

30 Z. Wang, *et al.*, Influence of laser surface remelting on microstructure and degradation mechanism in simulated body fluid of Zn-0.5Zr alloy, *J. Mater. Sci. Technol.*, 2019, **35**, 2705–2713, DOI: 10.1016/j.jmst.2019.05.019.

31 M. Wątroba, W. Bednarczyk, J. Kawałko and P. Bała, Effect of zirconium microaddition on the microstructure and mechanical properties of Zn-Zr alloys, *Mater. Charact.*, 2018, **142**, 187–194, DOI: 10.1016/j.matchar.2018.05.055.

32 P. Li, *et al.*, Investigation of zinc-copper alloys as potential materials for craniomaxillofacial osteosynthesis implants, *Mater. Sci. Eng., C*, 2019, **103**, 109826, DOI: 10.1016/j.msec.2019.109826.

33 H. F. Li, *et al.*, Development of biodegradable Zn-1X binary alloys with nutrient alloying elements Mg, Ca and Sr, *Sci. Rep.*, 2015, **5**, 10719, DOI: 10.1038/srep10719.

34 J. Bai, *et al.*, Mechanical Properties and Degradation Behaviors of Zn-xMg Alloy Fine Wires for Biomedical Applications, *Scanning*, 2021, 4831387, DOI: 10.1155/2021/4831387.

35 X. Liu, *et al.*, Effects of alloying elements (Ca and Sr) on microstructure, mechanical property and in vitro corrosion behavior of biodegradable Zn–1.5Mg alloy, *J. Alloys Compd.*, 2016, **664**, 444–452, DOI: 10.1016/j.jallcom.2015.10.116.

36 D. Hernández-Escobar, R. R. Unocic, M. Kawasaki and C. J. Boehlert, High-pressure torsion processing of Zn–3Mg alloy and its hybrid counterpart: A comparative study, *J. Alloys Compd.*, 2020, **831**, 154891, DOI: 10.1016/j.jallcom.2020.154891.

37 J.-W. Lee, *et al.*, Long-term clinical study and multiscale analysis of in vivo biodegradation mechanism of Mg alloy, *Proc. Natl. Acad. Sci. U. S. A.*, 2016, **113**, 716–721, DOI: 10.1073/pnas.1518238113.

38 N. Wang, *et al.*, Magnesium alloys for orthopedic applications:A review on the mechanisms driving bone healing, *J. Magnesium Alloys*, 2022, **10**, 3327–3353, DOI: 10.1016/j.jma.2022.11.014.

39 H. Jin, *et al.*, Novel high-strength, low-alloys Zn-Mg (<0.1wt% Mg) and their arterial biodegradation, *Mater. Sci. Eng., C*, 2018, **84**, 67–79, DOI: 10.1016/j.msec.2017.11.021.

40 E. Mostaed, M. Sikora-Jasinska, J. W. Drelich and M. Vedani, Zinc-based alloys for degradable vascular stent applications, *Acta Biomater.*, 2018, **71**, 1–23, DOI: 10.1016/j.actbio.2018.03.005.

41 J. Venezuela and M. S. Dargusch, The influence of alloying and fabrication techniques on the mechanical properties, biodegradability and biocompatibility of zinc: A comprehensive review, *Acta Biomater.*, 2019, **87**, 1–40, DOI: 10.1016/j.actbio.2019.01.035.

42 E. Mostaed, *et al.*, Novel Zn-based alloys for biodegradable stent applications: Design, development and in vitro degradation, *J. Mech. Behav. Biomed. Mater.*, 2016, **60**, 581–602, DOI: 10.1016/j.jmbbm.2016.03.018.

43 L.-Q. Wang, *et al.*, Microstructure, Mechanical Properties and Fracture Behavior of As-Extruded Zn–Mg Binary Alloys, *Acta Metall. Sin.*, 2017, **30**, 931–940, DOI: 10.1007/s40195-017-0585-4.

44 W. Pachla, *et al.*, Structural and mechanical aspects of hypoeutectic Zn-Mg binary alloys for biodegradable vascular stent applications, *Bioact. Mater.*, 2021, **6**, 26–44, DOI: 10.1016/j.bioactmat.2020.07.004.

45 P. Chi, *et al.*, A novel Mg-Zn-Nd-Zr alloy lumbar interbody fusion cage: An in vitro and in vivo study, *J. Magnesium Alloys*, 2025, **13**, 2651–2669, DOI: 10.1016/j.jma.2024.06.017.

46 X. Wan, *et al.*, Synergization of yield strength and ductility for a dilute Mg-Zn-Nd-Ca alloy through pinned twin boundary and Guinier–Preston zone, *J. Magnesium Alloys*, 2025, 3466–3486, DOI: 10.1016/j.jma.2025.04.027.

47 D. Natarajan, Z. Ye, L. Wang, L. Ge and J. L. Pathak, Rare earth smart nanomaterials for bone tissue engineering and implantology: Advances, challenges, and prospects, *Bioeng. Transl. Med.*, 2022, **7**, e10262, DOI: 10.1002/btm2.10262.

48 L. Ye, *et al.*, Effect of grain size and volume fraction of eutectic structure on mechanical properties and corrosion behavior of as-cast Zn–Mg binary alloys, *J. Mater. Res. Technol.*, 2022, **16**, 1673–1685, DOI: 10.1016/j.jmrt.2021.12.101.

49 Z. Zhu and A. D. Pelton, Critical assessment and optimization of phase diagrams and thermodynamic properties of RE–Zn systems-part I: Sc–Zn, La–Zn, Ce–Zn, Pr–Zn, Nd–Zn, Pm–Zn and Sm–Zn, *J. Alloys Compd.*, 2015, **641**, 249–260, DOI: 10.1016/j.jallcom.2015.03.140.

50 Z. Li, *et al.*, Suppression mechanism of initial pitting corrosion of pure Zn by Li alloying, *Corros. Sci.*, 2021, **189**, 109564, DOI: 10.1016/j.corsci.2021.109564.

51 N. Mollaei, S. M. Fatemi, M. R. Aboutalebi, S. H. Razavi and W. Bednarczyk, Dynamic recrystallization and deformation behavior of an extruded Zn-0.2 Mg biodegradable alloy, *J. Mater. Res. Technol.*, 2022, **19**, 4969–4985, DOI: 10.1016/j.jmrt.2022.06.159.

52 S. Liu, *et al.*, Dynamic recrystallization of pure zinc during high strain-rate compression at ambient temperature, *Mater. Sci. Eng., A*, 2020, **784**, 139325, DOI: 10.1016/j.msea.2020.139325.

53 K. Edalati and Z. Horita, Significance of homologous temperature in softening behavior and grain size of pure metals processed by high-pressure torsion, *Mater. Sci. Eng., A*, 2011, **528**, 7514–7523, DOI: 10.1016/j.msea.2011.06.080.

54 L. Wang, *et al.*, Effect of cumulative strain on the microstructural and mechanical properties of Zn-0.02 wt% Mg alloy wires during room-temperature drawing process, *J. Alloys Compd.*, 2018, **740**, 949–957, DOI: 10.1016/j.jallcom.2018.01.059.

55 Z. Zhu and A. D. Pelton, Critical assessment and optimization of phase diagrams and thermodynamic properties of RE–Zn systems – Part II – Y–Zn, Eu–Zn, Gd–Zn, Tb–Zn, Dy–Zn, Ho–Zn, Er–Zn, Tm–Zn, Yb–Zn and Lu–Zn, *J. Alloys Compd.*, 2015, **641**, 261–271, DOI: 10.1016/j.jallcom.2015.02.227.

56 K. Huang, K. Marthinsen, Q. Zhao and R. E. Logé, The double-edge effect of second-phase particles on the recrystallization behaviour and associated mechanical properties of metallic materials, *Prog. Mater. Sci.*, 2018, **92**, 284–359, DOI: 10.1016/j.pmatsci.2017.10.004.

57 Z. Zhang and D. L. Chen, Contribution of Orowan strengthening effect in particulate-reinforced metal matrix nanocomposites, *Mater. Sci. Eng., A*, 2008, **483–484**, 148–152, DOI: 10.1016/j.msea.2006.10.184.

58 C. Chen, *et al.*, Alloying design strategy for biodegradable zinc alloys based on first-principles study of solid solution strengthening, *Mater. Des.*, 2021, **204**, 109676, DOI: 10.1016/j.matdes.2021.109676.

59 N. Hansen, Hall–Petch relation and boundary strengthening, *Scr. Mater.*, 2004, **51**, 801–806, DOI: 10.1016/j.scriptamat.2004.06.002.

60 X. Huang, *et al.*, Enhancing mechanical strength, tribological properties, cytocompatibility, osteogenic differentiation, and antibacterial capacity of biodegradable Zn-5RE (RE = Nd, Y, and Ho) alloys for potential bone-implant application, *J. Mater. Res. Technol.*, 2024, **30**, 2865–2878, DOI: 10.1016/j.jmrt.2024.04.015.

61 Y. Lu, *et al.*, Additively Manufactured Biodegradable Zn-Based Porous Scaffolds to Suppress Osteosarcoma and Promote Osteogenesis, *Adv. Mater.*, 2024, 2410589, DOI: 10.1002/adma.202410589.

62 D. S. Brauer, E. Gentleman, D. F. Farrar, M. M. Stevens and R. G. Hill, Benefits and drawbacks of zinc in glass ionomer bone cements, *Biomed. Mater.*, 2011, **6**, 045007, DOI: 10.1088/1748-6041/6/4/045007.